ADVANCED MATERIALS
www.advmat.de

A Universal Biocompatible and Multifunctional Solid Electrolyte in p-Type and n-Type Organic Electrochemical Transistors for Complementary Circuits and Bioelectronic Interfaces

*Cindy G. Tang, Ruhua Wu, Yingjun Chen, Zhongliang Zhou, Qiang He, Ting Li, Xihu Wu, Kunqi Hou, Christina J. Kousseff, Iain McCulloch, and Wei Lin Leong**

The development of soft and flexible devices for collection of bioelectrical signals is gaining momentum for wearable and implantable applications. Among these devices, organic electrochemical transistors (OECTs) stand out due to their low operating voltage and large signal amplification capable of transducing weak biological signals. While liquid electrolytes have demonstrated efficacy in OECTs, they limit its operating temperature and pose challenges for electronic packaging due to potential leakage. Conversely, solid electrolytes offer advantages such as mechanical flexibility, robustness against environmental factors, and ability to bridge the interface between rigid dry electronics systems and soft wet biological tissues. However, few systems have demonstrated generality and compatibility with a wide range of state-of-the-art organic mixed ionic-electronic conductors (OMIECs). This paper introduces a highly stretchable, flexible, biocompatible, self-healable gelatin-based solid-state electrolyte, compatible with both *p*- and *n*-type OMIEC channels while maintaining high performance and excellent stability. Furthermore, this nonvolatile electrolyte is stable up to 120 °C and exhibits high ionic conductivity even in dry environment. Additionally, an OECT-based complementary inverter with a record-high normalized-gain of 228 V^{-1} and a corresponding ultralow static power consumption of 1 nW is demonstrated. These advancements pave the way for versatile applications ranging from bioelectronics to power-efficient implants.

1. Introduction

Research on organic electrochemical transistors (OECTs) has tremendously intensified in recent years, contributing to major developments in various fields and applications, including printed electronics,[1,2] logic circuits,[3] wearable electronics,[4] bioelectronics,[5,6] neuromorphic computing,[7] soft robotics,[8] and chemical.[9] or biological sensors.[10] This progress is primarily driven by the development of organic mixed ionic-electronic conductors (OMIECs) as they exhibit efficient volumetric doping–dedoping at low operating voltages (<1 V), making them ideal as channel materials for OECTs with large transconductance.[11–13] Furthermore, most OMIEC materials are biocompatible.[14] and can thus be used for fabrication of bioelectronic devices and biosensors with low power consumption and large signal amplification.

OMIECs are semiconducting polymers that generally consist of a conjugated backbone for electronic conductivity and can transport ions for efficient volumetric doping and de-doping when the electrolyte is gated in the OECT. In recent years, a popular design approach has been the incorporation of a glycolated side chain on OMIECs to improve their hydrophilicity and facilitate ionic penetration.[15] The efficacy of ion intercalation depends not only on the side-chain of the OMIEC but also on the nature of the ionic species and characteristics of the electrolyte.[12,16] An OMIEC material typically demonstrates ion selectivity depending on the ions' polarizability, size, charge state, hydration, solvent, and concentration.[17] Therefore, it is crucial to consider the OMIEC material and the electrolyte as an integrated system, as their interplay influences the doping or ion transport kinetics. The synthetic design of new OMIEC materials for OECTs are largely optimized for sodium chloride (NaCl) or phosphate buffered saline (PBS) liquid electrolytes due to their applications in biological environments.[15,18–20] However, the presence of volatile liquid components in OECTs hinders their long-term performance and stability. In contrast, ionic

C. G. Tang, R. Wu, Y. Chen, Z. Zhou, Q. He, T. Li, X. Wu, K. Hou, W. L. Leong
School of Electrical and Electronic Engineering
Nanyang Technological University
50 Nanyang Avenue, Singapore 639798, Singapore
E-mail: wlleong@ntu.edu.sg
C. J. Kousseff, I. McCulloch
Department of Chemistry
University of Oxford
Oxford OX1 3TA, UK
I. McCulloch
Andlinger Center for Energy and the Environment, and Department of Electrical and Computer Engineering
Princeton University
Princeton, NJ 08544, USA

The ORCID identification number(s) for the author(s) of this article can be found under https://doi.org/10.1002/adma.202405556

DOI: 10.1002/adma.202405556

liquids (ILs) offer nonvolatility, higher operating voltage, and improved thermal stability. Despite these advantages, the liquid nature of these electrolytes presents certain challenges, including difficulties in encapsulation using conventional printing techniques and susceptibility to leaks.

To address these issues, numerous solid or quasisolid electrolyte systems used in OECTs comprising of a host synthetic or natural polymer matrix with IL, salt, or humectant have been proposed. Examples of such electrolyte systems include biopolymers (e.g., chitosan.[21] or gelatin[22,23]) and synthetic polymers (e.g., poly(vinylidene fluoride-*co*-hexafluoropropylene) (PVDF-*co*-HFP),[5,24] poly(ethylene glycol) diacrylate (PEGDA),[25,26] thermoplastic polyurethane (TPU),[27] poly(*N*-isopropylacrylamide) (PNIPAm),[28,29] poly(glycerol 1,3-diglycerolate diacrylate) poly(DGLY),[30] or poly(sodium-4-styrene sulfonate (PSSNa)[31,32]) incorporated with *d*-sorbitol, glycerol and/or an ionic compound such as 1-ethyl-3-methylimidazolium ($[EMIM]^+$) cation and bis(trifluoromethylsulfonyl)imide ($[TFSI]^-$), tetrafluoroborate ($[BF_4]^-$), or ethyl sulfate ($[EtSO_4]^-$) anions. The limitation of using polyelectrolytes is the supply of only a single type of mobile ion (e.g., anions in polyquaternium-10 (PQ-10) or cations in PSSNa.[31]). For complementary electronic circuitries, two different polyelectrolytes with suitable anions and cations are therefore needed for respective *p*- and *n*-type devices, further creating additional fabrication complexity. To enable facile processing that can promote easy integration into printed electronics for large-scale fabrication of small footprint OECTs with more complex circuitry,[31,33,34] it is highly desirable to use a single solid electrolyte system for both *p*- and *n*-type OECTs. Only a small handful of solid electrolyte systems have gated both *p*- and *n*-type OECTs.[21,27,30] The workhorse n-type OMIEC polymer, poly(benzimidazobenzophenanthroline) (BBL), permits penetration of both hydrophilic and hydrophobic cations and has been demonstrated to work well with various electrolyte systems.[27,31,35] However, with the emergence of new *n*-type OMIECs[36] particularly those with glycolated or mixed alkyl/glycol-based side chains that facilitates ion penetration, hydrophobic cations are unable to inject well into these materials (e.g., $[EMIM]^+$-based solid electrolyte systems are ineffective in performing volumetric doping of a naphthalene diimide–thiophene-based (NDI-T) OMIEC polymer functionalized with mixed alkyl-ethylene glycol side chain as observed by Zhong et al.[30] and in this work, vide infra).

In this study, we developed a gelatin-based ionogel incorporated with a biocompatible ionic liquid, tris(2-hydroxyethyl)-methylammonium methylsulfate ($[MTEOA][MeOSO_3]$), as the ion conductor. The hydroxyl groups on the ammonium cation and short alkyl chain on the sulfate anion imparts sufficient hydrophilicity to promote efficient ion injection into both *p*- and *n*-type OMIECs, particularly those with glycolated or mixed alkyl/glycol-based side chains. Furthermore, unlike ILs containing $[BF_4]^-$, hexafluorophosphate ($[PF_6]^-$), or hexafluoroantimonate ($[SbF_6]^-$) anions that hydrolyze in the presence of water to form highly hazardous and corrosive hydrogen fluoride,[37] $[MTEOA][MeOSO_3]$ remains stable and miscible with water. $[MTEOA][MeOSO_3]$ is classified as a third-generation IL that is characterized by their low environmental toxicity, biocompatibility, biodegradability, and renewable nature rendering them highly suitable for potential biomedical applications.[38] Additionally, cytotoxicity assessment of $[MTEOA][MeOSO_3]$ reveals that it is nontoxic to human skin cells, thereby making it viable for on-skin electronic devices.[39]

Furthermore, contrary to synthetic polymers, natural biomaterials are greener and abundant in nature, compatible with biological systems, and low-cost. In particular, gelatin—primarily used in food, pharmaceutical, and cosmetic industries as a gelling agent due to the formation of interchain hydrogen bonds—is a good candidate as a host matrix. The polyampholytic gelatin comprise a variety of polar, nonpolar, charged and uncharged amino acids where glycine, proline, and hydroxyproline are the most abundant.[40] Hydrogel or gel-based electrolytes made from biopolymers, such as chitosan[21] or gelatin[22,23] blended with water or glycerol have been reported for use in OECTs and demonstrate pH or humidity-sensing capabilities. However, they generally suffer from poor ionic conductivity which reduces the response time of the OECTs. Moreover, the environmental sensitivity of these electrolytes toward changes in temperature or humidity limits the reliability of the OECTs where long-term stable output is required, particularly in integrated circuits.

Herein, we demonstrated a biocompatible, biodegradable, highly flexible, and stretchable gelatin–$[MTEOA][MeOSO_3]$ solid electrolyte system compatible with a wide range OMIECs to achieve highly stable OECTs with good electrochemical response. This single solid electrolyte system can efficiently inject ions into both *p*- and *n*-type OECTs thus reducing the fabrication complexity of OECT-based integrated circuits. Furthermore, a reliable OECT operation was demonstrated, where the device is robust toward damage due to its self-healing nature and high temperature resilience of up to 120 °C. Remarkably, we attained a complementary inverter with ultralow static power consumption (1 nW) and, to the best of our knowledge, a highest reported supply-voltage normalized gain (228 V^{-1}) for an all-solid-state OECT-based inverter. This advancement opens many possibilities for application of all solid-state OECTs in logic circuits, wearable and implantable device applications and bring flexible OECTs a step closer toward commercialization.

2. Results and Discussion

2.1. Universal Solid-State Electrolyte for Organic Electrochemical Transistors

To demonstrate the generality of gelatin–$[MTEOA][MeOSO_3]$ solid electrolyte with a wide range of *p*- and *n*-type OMIEC materials (see Figure S1 for a list of materials tested and their corresponding chemical structures, Supporting Information), a comparison of the OECT performance with a commonly used liquid electrolyte (0.1 M aqueous NaCl) and various state-of-the-art solid electrolytes (PVDF-*co*-HFP–$[EMIM][BF_4]$, and PVDF-*co*-HFP–[EMIM][TFSI]) were carried out. The device architecture of the OECT with coplanar source–drain-gate electrodes is shown in **Figure 1a**. The gelatin–$[MTEOA][MeOSO_3]$ solid electrolyte (or ionogel) was prepared by solution-casting a heated and liquified aqueous mixture of gelatin– $[MTEOA][MeOSO_3]$ followed by annealing to remove water present in the electrolyte. The solid electrolyte ionogel films were left to gelate and solidify in ambient air for at least 16 h before testing (Figure S2, Supporting

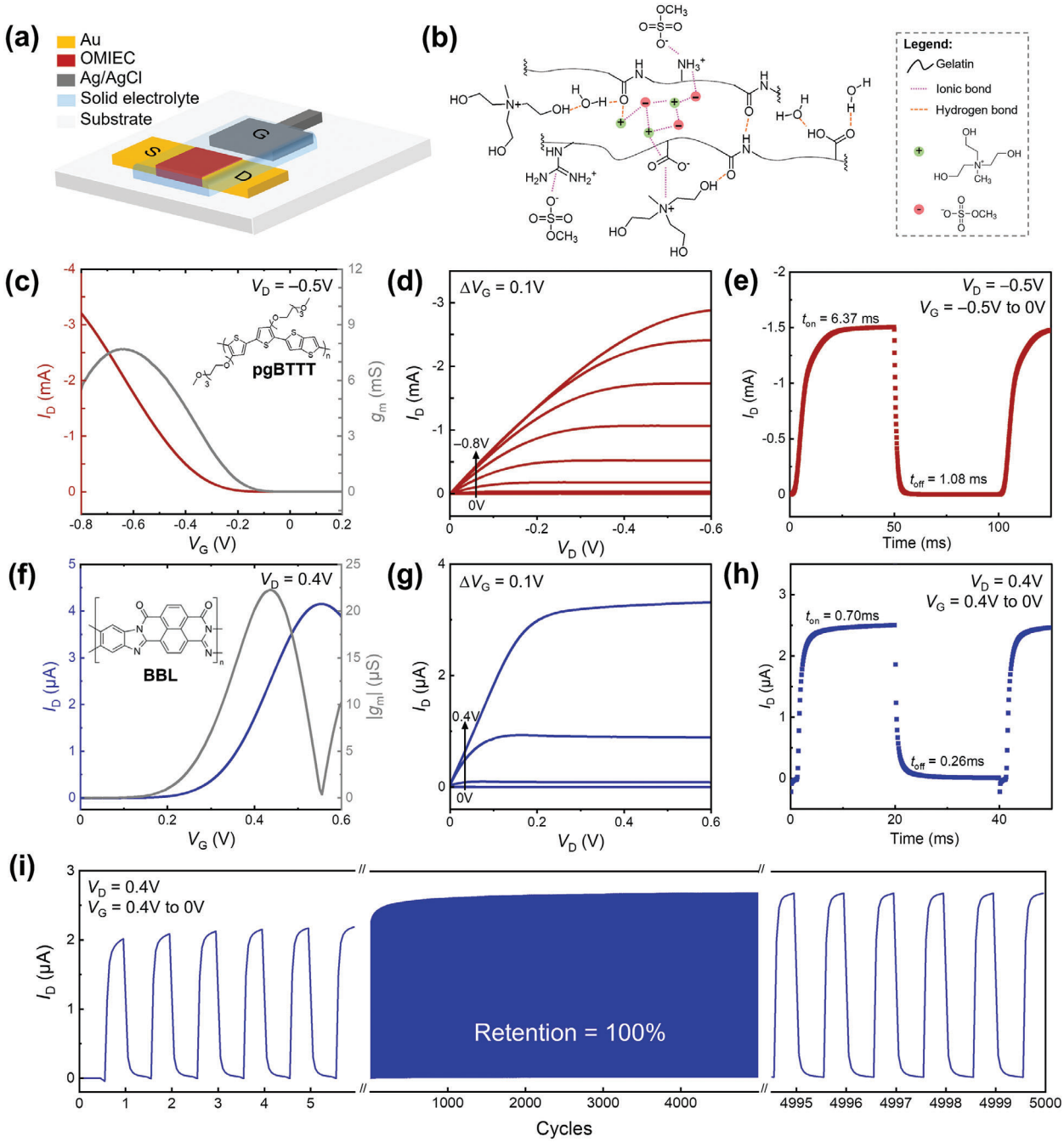

Figure 1. *p*- and *n*-type OECTs with gelatin–[MTEOA][$MeOSO_3$] solid electrolyte. a) Schematic diagram of an all-solid-state OECT with coplanar source–drain-gate electrodes. b) Schematic representation of the possible ionic interactions and hydrogen bonds between gelatin and [MTEOA][$MeOSO_3$]. c) Transfer and transconductance (forward scan, from 0.2 to –0.8 V), d) output, and e) transient response of pgBTTT. f) Transfer and transconductance (forward scan, from 0 to 0.6 V), g) output, and h) transient response of BBL. Chemical structures of the respective channel materials are shown in inset of c) and f). i) Cycling stability of BBL OECT at a frequency of 50 Hz and duty cycle of 50%. The measured channel dimensions (*W*/ *L*/ *d*) were 97 μm/ 12 μm/ 47 nm and 110 μm/ 12 μm/ 36 nm for pgBTTT and BBL OECTs, respectively.

Information). If water solvent is not removed, the presence of excess bulk water in the gelatin–[MTEOA][$MeOSO_3$] hydrogel would increase the volatility of the electrolyte as water can evaporate from the system over time thereby causing changes to its electrical and mechanical properties (e.g., reduced elasticity), limit the electrochemical stability window of the electrolyte, and the hydrogel would turn from a solid-to-liquid state at a lower melting temperature (T_m) (vide infra).

The hydrophilic nature of the protic IL (Figure S3a,b, Supporting Information), due to the presence of hydroxyl groups on $[MTEOA]^+$ cation and polar $[MeOSO_3]^-$ anion, facilitates effective ion penetration and efficient ion transport within

numerous ionophilic and hydrophilic *p*- and *n*-type OMIEC polymers. A schematic representing the possible ionic and hydrogen bonding interactions between the IL, adsorbed water molecules and charged groups (carboxylate and ammonium groups) on the polyampholyte gelatin is shown in Figure 1b. Despite water adsorption by the [MTEOA][$MeOSO_3$] IL, its electrochemical stability window remains larger than that of an aqueous electrolyte system (Figure S3c, Supporting Information).

For *p*-type enhancement-mode OECTs, upon applying a negative gate bias (V_G), holes are induced at the polymeric channel and counter-balanced by anions that are injected from the solid electrolyte thus giving rise to a *p*-doped channel and an increased drain current (I_D) measured by applying a voltage (V_D) between the drain and source electrodes. Similarly for *n*-type enhancement-mode OECTs or *p*-type depletion-mode OECTs, upon applying a positive V_G, cations are injected into the channel. The transfer, transconductance (g_m) and output characteristic of a representative hydrophilic *p*-type accumulation-mode poly(2-(4,4'-bis(2-methoxyethoxy)-5'-methyl-[2,2'bithiophen]-5-yl)-5-methylthieno[3,2-b]thiophene) (pgBTTT)-based OECT using gelatin–[MTEOA][$MeOSO_3$] solid electrolyte is presented in Figure 1c–e. Typical pinch-off behaviors were observed in the corresponding output characteristic. The transconductance, which is the derivative of the transfer curve ($g_m = \partial I_D/\partial V_G$), can be used to determine the electronic charge carrier mobility (μ) and volumetric capacitance (C^*) for an OECT. μC^* is often employed as the OMIEC material system figure-of-merit as it reflects the charge storage capacity, ionic, and electronic charge transport of the material. It can be extracted from the peak transconductance in the saturation regime by the Bernards and Malliaras model[41] using $g_{max} = \frac{Wd}{L}\mu C^*|(V_T - V_G)|$, where V_T is the threshold voltage, and W, L, and d are the channel width, length, and thickness, respectively. A large μC^* of 438 F cm^{-1} V^{-1} s^{-1} was obtained for gelatin–[MTEOA][$MeOSO_3$] (80 wt%) in contrast to 316, 211, and 369 F cm^{-1} V^{-1} s^{-1} for aqueous 0.1 M NaCl electrolyte, PVDF-*co*-HFP–[EMIM][BF_4] (80 wt%), and PVDF-*co*-HFP–[EMIM][TFSI] (80 wt%) solid electrolytes, respectively (Figure S4, Supporting Information). Large μC^* translates to high g_m, thereby enabling effective signal amplification particularly for small biological signals in biosensing applications. A similar trend wherein the gelatin–[MTEOA][$MeOSO_3$] solid electrolyte presented the largest μC^* compared to other electrolytes tested was observed with various *p*- and *n*-type OMIEC materials—poly(2-(3,3'-monoethyleneglycol monomethyl ether)-[2,2'-bithiophen]-5yl)-alt-(2-(3,3'-pentaethyleneglycol monomethyl ether)-[2,2'-bithiophen]-5yl) (p(g1T2-g5T2)).[42] and poly-(2,7-di(2,5,8,11-tetraoxaheptadecan-17-yl)-4-(thiophen-2-yl)benzo[lmn][3,8]phenanthroline-1,3,6,8(2H,7H)-tetraone) (p(C_6NDI-T)).[43] (Figures S5 and S6, Supporting Information). Furthermore, a large μC^* of 78 F cm^{-1} V^{-1} s^{-1} for gelatin–[MTEOA][$MeOSO_3$] versus 24 F cm^{-1} V^{-1} s^{-1} for NaCl was obtained with poly(3-(5-carboxypentyl) thiophene-2,5-diyl) (P3CPT) (Figure S7, Supporting Information), a *p*-type OMIEC material with hydrophilic carboxylic acid-functionalized side chain.

For BBL, a side-chain-free *n*-type ladder-polymer, the ingress of a relatively large cation [MTEOA]$^+$ compared to a smaller cation Na^+ during *n*-doping led to lowered μC^* (Figure 1f,g; and Figure S8, Supporting Information). This can be attributed to a reduction in μ from 1.4×10^{-2} to 5.3×10^{-3} cm^2 V^{-1} s^{-1}, possibly due to a disruption in crystalline order with penetration of the large cation. However, the transient response on time (t_{on})—characterized by the slower switching process from an off-state to an on-state—of the BBL OECT with gelatin–[MTEOA][$MeOSO_3$] (Figure 1h) remained comparable to operation in aqueous NaCl electrolyte and is faster than [EMIM]$^+$. The fast transient response was likely due to a lamellar expansion of the BBL film caused by water retention upon electrochemical doping by the hydrophilic solid electrolyte hence facilitating transport of the hydrophilic ions. A similar phenomena was observed in aqueous NaCl electrolyte.[35] Furthermore, t_{on} normalized by channel geometry ($d\sqrt{WL}$) was significantly faster for many OMIECs with gelatin–[MTEOA][$MeOSO_3$] compared to the other solid electrolytes by up to ≈15x (Table S1, Supporting Information). However, for strongly hydrophobic polymer with alkylated side chains, such as poly((5-fluoro-2,1,3-benzothiadiazole-4,7-diyl)(4,4-dihexadecyl-4H-c2,1-b:3,4-b']dithiophene-2,6-diyl)(6-fluoro-2,1,3-benzothiadiazole-4,7-diyl)(4,4-dihexadecyl-4H-cyclopenta[2,1-b:3,4b'] dithiophene-2,6-diyl)) (PCDTFBT) (Figure S9, Supporting Information), a large ion injection barrier was evident from the increased V_T and slow transient response time observed with gelatin–[MTEOA][$MeOSO_3$] as compared to a hydrophobic electrolyte PVDF-*co*-HFP–[EMIM][TFSI].[5] These results highlight the ability of [MTEOA]$^+$ or [$MeOSO_3$]$^-$ ions to efficiently inject and transport within hydrophilic conjugated polymers, particularly those comprising polar oligoether side chain which constitutes a large body of work for state-of-the-art OMIECs tailored for OECTs.[15]

Additionally, devices with gelatin–[MTEOA][$MeOSO_3$] demonstrated superior cycling and storage stability compared to other solid electrolytes. The cycling stability was determined by applying a continuous pulse gate potential across the same duration and up to 20 000 cycles for different electrolytes and comparing their maximum current retention ($I_D/I_{D,max}$) (Table S1, Supporting Information). Such cycling tests accelerates the aging of the OECTs by either excessive swelling, side reactions or bias stress during the repeated doping–dedoping process.[44] The OMIEC film experiences volumetric deformation during ion penetration and the extent of deformation depends on the hydration and size of the dopant ion.[45] The size of the cations and anions tested here are of the following order: [MTEOA]$^+$ > [EMIM]$^+$ > Na^+ and [TFSI]$^-$ > [$MeOSO_3$]$^-$ > [BF_4]$^-$ > Cl^- (Figure S10, Supporting Information). Despite the relatively large size of [MTEOA]$^+$ or [$MeOSO_3$]$^-$, the gelatin–[MTEOA][$MeOSO_3$] system had a higher or comparable current retention compared to the other solid electrolytes tested for all the *p*- and *n*-type OMIEC systems—P3CPT, p(g1T2-g5T2), pgBTTT, poly(3,4-ethylenedioxythiophene)-poly(styrenesulfonate) (PEDOT:PSS) (Figure S11, Supporting Information), BBL, and p(C_6NDI-T). For instance, $I_D/I_{D,max}$ for P3CPT-based OECTs were 92%, 83%, 72%, and 70% for gelatin–[MTEOA][$MeOSO_3$], 0.1 M aqueous NaCl, PVDF-*co*-HFP–[EMIM][BF_4], and PVDF-*co*-HFP–[EMIM][TFSI], respectively. Remarkably, the gelatin–[MTEOA][$MeOSO_3$] devices also demonstrated good storage stability as it maintained a high on-off ratio of ≈10^6 after being stored for 2 months in ambient air (24 °C, relative humidity (R.H.) 65%) and further presented the smallest change in transconductance compared to other solid electrolytes (Figure S12, Supporting Information).

High cycling and storage stability are critical for commercialization of OECTs where long-term stability and repeatability is key. These results demonstrates that gelatin–[MTEOA][$MeOSO_3$] is a stable and universal solid electrolyte system suitable for efficient charge injection and transport in OMIECs to construct high performance OECTs.

2.2. Characterization of Gelatin-MSO Electrolyte

Besides the hydrophilic nature of $[MTEOA]^+$ or $[MeOSO_3]^-$ which favors the injection of these ions into the OMIEC channel, the improved doping kinetics can be also attributed to a high conductivity (σ) of the electrolyte. The conductivities of the gelatin-IL solid electrolyte composites, determined by electrical impedance spectroscopic (EIS) measurements, as a function of the mass ratio of the IL is presented in **Figure 2a**. Depending on the mass ratio (wt%) of [MTEOA][$MeOSO_3$] in the system, distinct regimes of conductivity corresponding to a predominant hydronium/hydroxide conduction, ionic conduction, or a mix of both is evident. In ambient air (24 °C, R.H. 65%), σ of the gelatin–[MTEOA][$MeOSO_3$] (80 wt%) ionogel ($\sigma_{80wt\%} = 6.3 \times 10^{-4}$ S cm^{-1}) is nearly 5 orders of magnitude larger than pristine gelatin, ≈3 order of magnitude larger than previously reported gelatin-glycerol hydrogel[23] and similar to other polymer/IL solid electrolyte systems[27,46,47] used in OECTs (Table S2, Supporting Information). The conductivity at low IL content (≤ 40 wt% IL) strongly depends on the humidity of the environment thus suggesting that hydronium (proton) or hydroxide conduction is dominant. A drastic increase in conductivity by 10^2–10^4 orders of magnitude was observed from dry nitrogen (N_2) to ambient air due to physically adsorbed water molecules that forms a network of hydrogen bonds which facilitates the transport of hydronium or hydroxide. At ≥ 67 wt% IL, σ becomes nearly invariant with increased IL content and has a weak dependence on humidity. The change in σ of gelatin–[MTEOA][$MeOSO_3$] (80 wt%) across different humidities from R.H. 0% to 86% is approximately one order of magnitude (Figure S13a, Supporting Information). This suggests σ is largely dominated by the ionic conductivity (σ_{ionic}) contributed by the high content of cations and anions from the IL.

Since σ_{ionic} dominates at higher IL content, σ remains relatively invariant at elevated temperatures as it is less susceptible to the desorption of water molecules that leads to lower hydronium/hydroxide conduction. This is evident at a high IL mass ratio of ≥80 wt% in air where the overall σ is nearly independent of temperature (Figure 2b). In contrast, at lower ratio of 50 wt% IL, an apparent negative activation energy accompanied by a decrease in σ between 25 and 90 °C was observed. The temperature dependence of σ in N_2 (Figure S13b, Supporting Information) is well-described by the Arrhenius equation $\sigma = \sigma_0 \, e^{-\frac{E_a}{k_B T}}$ in the temperature range of 25–80 °C, where σ_0 is the pre-exponential factor, E_a is the activation energy, k_B is the Boltzmann's constant, and T is temperature. The fitted E_a values (Table S3, Supporting Information) decrease with increasing IL content from 0.55 eV for pristine gelatin to 0.19 eV for 80 wt% IL, suggesting that the energy barrier to ionic transport reduces. Low E_a leads to reduced fluctuation in σ with changing temperature conditions. Relatively stable OECT operation across a high temperature range of 25–120°C (Figure 2c) was demonstrated with gelatin–[MTEOA][$MeOSO_3$] (80 wt%) and a thermally stable p(g1T2-g5T2) channel.[26] Although a small increase in threshold voltage of up to 68 mV (Figure 2d; and Figure S14, Supporting Information) was observed as the temperature increased from room temperature up to 80 °C, the transfer characteristics displayed almost no hysteresis with negligible changes in I_D. The transient response, on the other hand, is highly sensitive toward changes in conductivity of the electrolyte—a gradual dehydration lead to a decrease in σ by 2.3-fold with a corresponding 2.7-fold increase in t_{on}. At even higher temperatures from 80 to 120 °C, the increased thermal energy of the ions enhances the overall conductivity leading to faster t_{on}.

Employing gelatin electrolytes with different mass ratios of IL in pgBTTT-based OECT shows a systematic increase in I_D, lowered V_T and reduced hysteresis as the IL content increases (Figure 2e). Though unsurprising, these results underscore the importance of a sufficiently large ionic reservoir required to provide a supply of ions for efficient injection into the OECT channel. The shift in V_T can be ascribed to a reduction in potential drop across the nonpolarizable silver/silver chloride (Ag/AgCl) gate–electrolyte interface with increased ionic content as previously reported for a PEDOT:PSS-based OECT operating in aqueous NaCl electrolyte.[48] Therefore, to achieve high-speed OECTs stable across a larger temperature range, an optimum mass ratio of gelatin–[MTEOA][$MeOSO_3$] (80 wt%) was selected for all device characterizations, unless otherwise stated, due to its ability to maintain an elastic solid compared to higher IL mass ratio (89 wt%) which has a viscous liquid appearance. A range of other water-soluble polymers were mixed with [MTEOA][$MeOSO_3$] (80 wt%) to form ionogels. However, these ionogels maintained as a viscous liquid instead of solidifying or its polymer matrix had phase segregated from the IL (Figure S15, Supporting Information).

To rationalize the relatively invariant conductivity of gelatin–[MTEOA][$MeOSO_3$] solid electrolyte at high IL content, we further study the interaction of the IL with gelatin and its organization within the gelatin host matrix. A high glass transition temperature (T_g) was observed for pure gelatin (41°C) (Figure S16, Supporting Information) which stems from strong inter/intramolecular hydrogen bond interactions by the amide bonds. The pure gelatin sample was pre-processed following the same protocol as the gelatin–[MTEOA][$MeOSO_3$] ionogel. Attenuated total reflectance (ATR)—Fourier transform infrared (FTIR) spectroscopy was used to probe the amide bands in gelatin that are sensitive to hydrogen-bonding, dipole–dipole interactions, and conformational changes (Figure 2f). The observed amide–I and amide–II bands, corresponding to the stretching vibration (ν) of the amide carbonyl C═O groups and to a combination of N—H bending vibration (δ) and ν(C—N) of the amide groups along the polypeptide backbone, were found respectively at 1630 and 1532 cm^{-1} for the pure gelatin which is characteristic of denaturation of the crystalline triple helix.[49] This is in agreement with the X-ray diffraction (XRD) pattern that indicates gelatin is amorphous (Figure S17, Supporting Information). The addition of [MTEOA][$MeOSO_3$] disrupts the inter/intramolecular hydrogen bonds in gelatin, evident from the blueshifted amide–I and –II bands to 1645 and 1551 cm^{-1}, respectively, due to effectively shortened C═O, N—H, or C—N

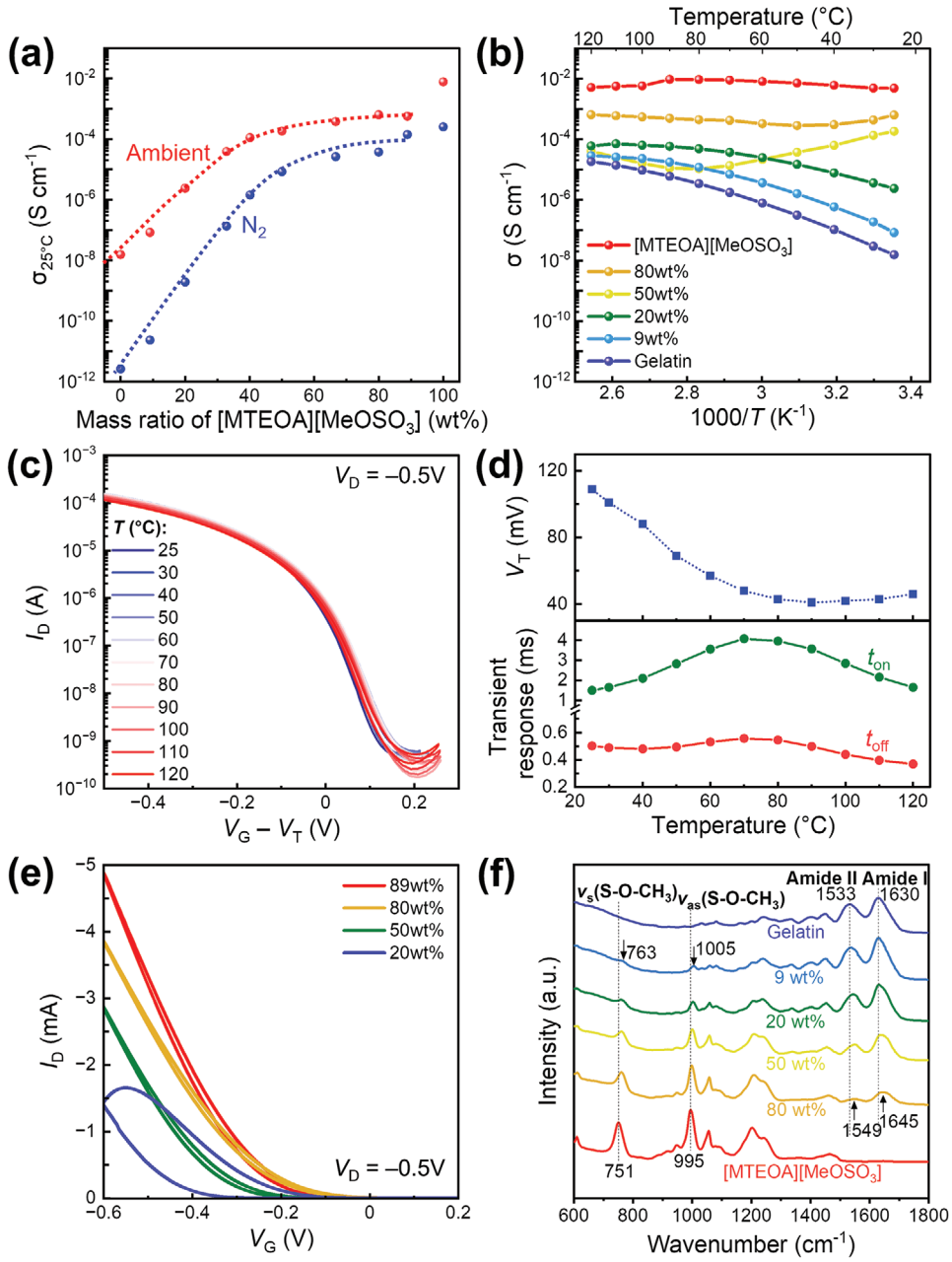

Figure 2. Characterization of gelatin–[MTEOA][MeOSO3] solid electrolyte. Conductivity of a) pure [MTEOA][$MeOSO_3$] IL, gelatin, and gelatin–[MTEOA][$MeOSO_3$] solid electrolyte with different mass ratios (wt%) of IL at 25 °C, and b) at various temperatures (T) in ambient air. Influence of temperature on p(g1T2-g5T2)-based OECT (W/L/d = 110 µm/12 µm/ 15 nm) with gelatin–[MTEOA][$MeOSO_3$] (80 wt%) on its c) transfer characteristics, d) threshold voltage (V_T), and transient response (t_{on} and t_{off}) conducted with V_G square voltage varying from 0 to –0.5 V and V_D = –0.5 V. e) Transfer characteristics of pgBTTT-based OECT (W/L/d = 106 µm/53 µm/47 nm) gelatin electrolyte with different IL mass ratios at V_D = –0.5 V. f) ATR-FTIR spectra of gelatin, gelatin-[MTEOA][$MeOSO_3$] solid electrolyte with different IL mass ratios and [MTEOA][$MeOSO_3$] IL.

bonds which translate to absorption peaks at higher frequencies. The weakened hydrogen bond network within the polymer also reduces T_g of gelatin–[MTEOA][$MeOSO_3$] ($T_g \leqslant 13$°C upon addition of more than 33 wt% IL). A deconvolution of the symmetric stretching vibration band of S—O—CH_3 (ν(S—O)) from [$MeOSO_3$]$^-$ (Figure S18, Supporting Information), by a sum of two Gaussian functions that represents the interaction of [$MeOSO_3$]$^-$ within the bulk IL and gelatin matrix respectively, showed a shift from 751 cm^{-1} in the bulk IL to 763 cm^{-1} in the gelatin matrix. This blueshift implies a stronger ionic interaction[50] of [$MeOSO_3$]$^-$ within the gelatin host. Increasing the IL content gave rise to a larger ratio of weakly interacting [$MeOSO_3$]$^-$ which may play a role in enhancing the overall ionic conductivity of the system. In addition, compared to gelatin or gelatin–[MTEOA][$MeOSO_3$] hydrogels which have T_m between 37 and 40 °C, the gelatin–[MTEOA][$MeOSO_3$] (80 wt%) ionogel

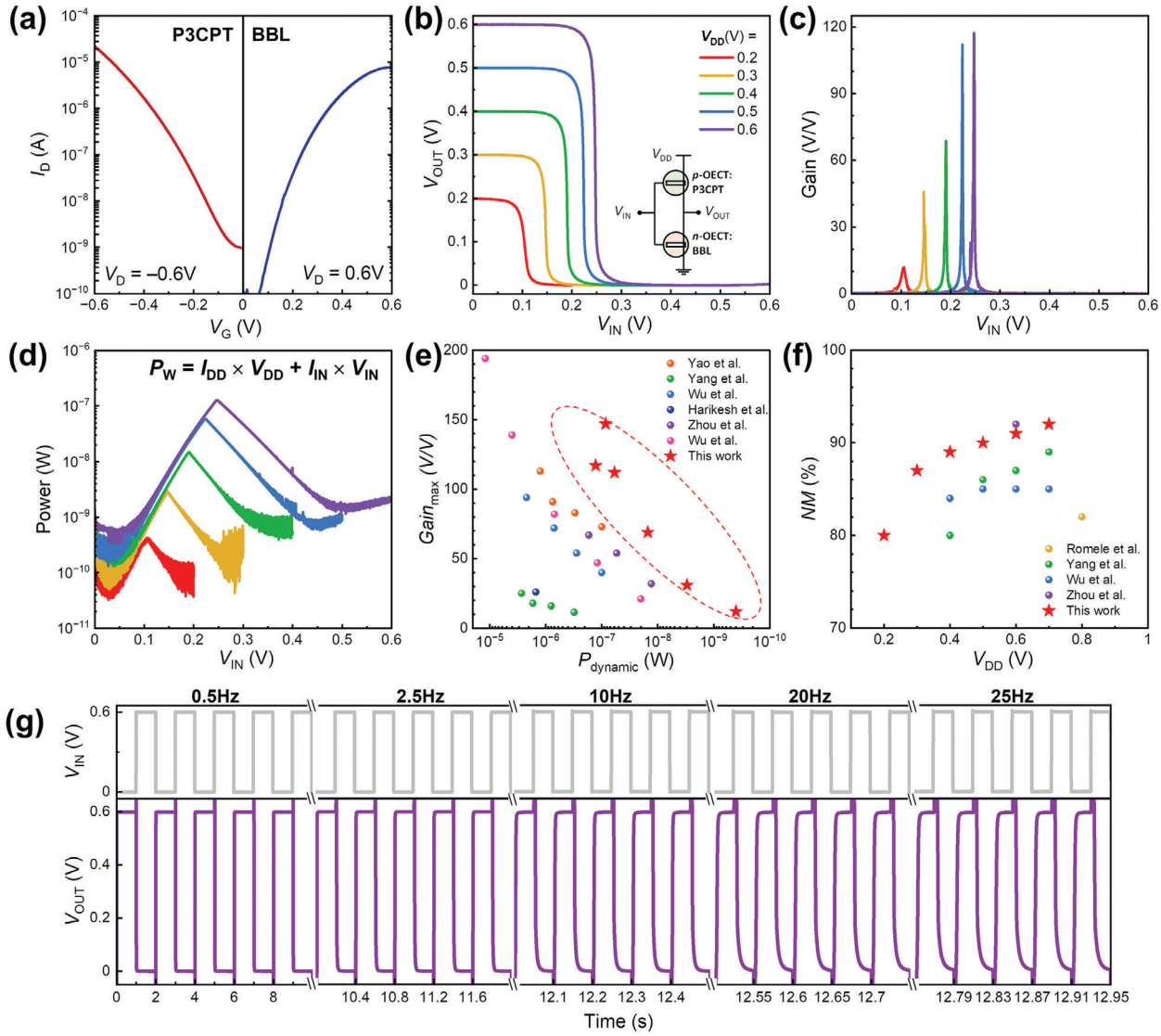

Figure 3. Complementary inverter with *p*-type P3CPT OECT ($W/L/d$ = 109 µm/ 17 µm/ 35 nm), *n*-type BBL OECT ($W/L/d$ = 108 µm/ 11 µm/ 36 nm) and gelatin–[MTEOA][$MeOSO_3$] solid electrolyte. a) Transfer curves of balanced *p*- and *n*-type characteristics. b) Voltage transfer characteristics (inset: circuit schematic), c) voltage gain, and d) power consumption of the complementary inverter at various supply voltages (V_{DD}). Benchmarking of OECT-based inverters in this work against those previously reported, in terms of e) peak gain values and f) noise margins.[7,31,48,53–56] g) Dynamic performance of the inverter at V_{DD} = +0.6 V over a frequency range from 0.5 to 25 Hz.

has an increased T_m of 49 °C (Figure S19, Supporting Information). To summarize, gelatin–[MTEOA][$MeOSO_3$] (80 wt%) ionogel's relatively high and invariant σ at operating temperatures between 25–120 °C (which is above its T_g) arises from it being an amorphous solid in a rubbery state up to its T_m, and a viscous liquid at temperatures above T_m. In both states, the polymer chain segments are flexible and can efficiently transport ions.

2.3. Low-Power Ultrahigh-Gain OECT-Based Inverter

Low-voltage and low-power operation of organic electronics is pivotal for its widespread adoption in battery-powered or even battery-less wearable systems and internet-of-things (IoT) applications.[51] Here, we demonstrate a high-gain ultralow-power complementary inverter comprising a pair of well-balanced enhancement-mode *p*- and *n*-type OECTs (**Figure 3a**), using a single solid electrolyte for both *p*-channel P3CPT and *n*-channel BBL. The complementary inverter is often used as a testbed to assess its feasibility as a fundamental building block in the construction of more complex circuits for both digital and analog applications. A schematic of the OECT-based complementary inverter is shown in the inset of Figure 3b. The input voltage (V_{IN}) is connected to the gate terminals of both OECTs, while the output voltage (V_{OUT}) is measured between the series connection of the transistors.

The voltage transfer characteristics (VTC) of the fabricated complementary inverter exhibited rail-to-rail voltage output

between a supply voltage (V_{DD}) of 0.2–0.6 V, even in the subthreshold region at V_{DD} = 0.2 V (Figure 3b,c). At V_{DD} = 0.5 V, the inverter has a V_{DD}–normalized gain of 228 V^{-1} (Table S4, Supporting Information), which is the highest reported for solid-state complementary OECT inverters. At higher V_{DD}, the switching voltage (V_{SW}) of the inverter begins to deviate from the ideal value of $V_{DD}/2$ but its gain remained high (216 V^{-1} at V_{DD} = 0.7 V) (Figure S20, Supporting Information). Deviation from the ideal inverter characteristics is possibly attributed to the antiambipolar behavior of BBL as the channel conductance decreases at high doping levels at high V_G (or V_{IN}).[52]

There had been numerous efforts to balance the trade-off between power and performance[53,55,56] as the inverter consumes less power at lower supply voltage at the expense of its gain. Few studies, however, had demonstrated ultralow power while maintaining a high performance. The maximum static power consumption (P_{static}) of the inverter reported in this work is very small—between 100 pW and 2 nW for V_{DD} = 0.2 and 0.6 V (Figure 3d), respectively. During switching of the inverter, the maximum dynamic power consumption ($P_{dynamic}$) per logic gate is only between 400 pW and 128 nW for V_{DD} = 0.2 and 0.6 V, respectively. Compared with inverters based on unipolar OECT and resistor ladder (P_{static} = 1.18 mW) that were implemented in printed large-scale digital circuits, such as shift registers and binary-coded decimal decoders,[57] a reduction in power consumption of up to 6 orders of magnitude is expected. These record high gain values and ultralow power consumption outperforms previous reported state-of-the-art planar- or vertical-OECT-based inverters (Figure 3e). Such low operational power consumption are beneficial for next-generation wearable electronics self-powered by light, heat, kinetic energy, radio frequency energy, biomass energy, and other energy sources that can only provide limited power supply.

Another parameter related to the inverter's VTC is the noise margin (*NM*) which determines the robustness of a logic circuit, wherein the higher the noise margin, the more reliable the circuit is against spurious signals. The noise margin of the low (NM_L) and high states (NM_H) are given by $NM_L = V_{IL}$ and $NM_H = V_{DD} - V_{IH}$, where V_{IL} and V_{IH} are the input voltages corresponding to the low and high states extracted from the inverter's VTC points at which the $\frac{\partial V_{OUT}}{\partial V_{IN}} = -1$. Table S4 (Supporting Information) summarizes the performances of the key figures of merit for the inverters reported here compared to the state-of-the-art OECT-based inverters. Respective NM_L and NM_H values of 0.217 and 0.329 V were achieved for V_{DD} = 0.6 V, thus presenting an overall percentage *NM* of 91% given by $(NM_L + NM_H)/V_{DD}$. The *NM* reported in this work at various operating voltages are among the highest reported values (Figure 3f). Additionally, Figure 3g shows stable rail-to-rail V_{OUT} swings at up to 25 Hz and the transient characteristics of the inverter is similar to the individual OECTs (Figure S21, Supporting Information).

2.4. Flexible, Stretchable and Self-Healing Bioelectronics

The biocompatible gelatin–[MTEOA][$MeOSO_3$] ionogel films developed here is ideal for wearable/skin-compatible electrophysiological signal monitoring and amplification. This ionogel was found to be highly stretchable (**Figure** 4a), has an elongation at break (ϵ_{max}) of 530% and exhibits a low Young's modulus of 7 kPa (Figure 4b). The film also displayed excellent fatigue resistance, retaining over 96% of maximum stress with no hysteresis upon 100 consecutive cycles with 180% strain (Figure S22, Supporting Information). Furthermore, the film demonstrates autonomous self-healing capability. Samples were cut into half and placed back into contact at room temperature (24 °C) or at skin surface temperature (35 °C) for 1 h before being stored and tested at room temperature 72 h later. The ϵ_{max} of the self-healed gelatin–[MTEOA][$MeOSO_3$] ionogel at room temperature and skin surface temperature were 228% and 410%, respectively. The self-healing efficiency (η), defined as the ratio of ϵ_{max} of the healed sample to that of the original sample, at 24 and 35 °C was only 43% and 77%, respectively, due to the absence of abundant free water which is vital to the self-healing mechanism of gelatin.[58] The self-healing process for the ionogel was fast and maximum η at room temperature can be attained within 20 min (Figure S23a, Supporting Information). Tensile measurements of gelatin–[MTEOA][$MeOSO_3$] hydrogels shows that the presence of water in the hydrogel aided the self-healing to a nearly full recovery (η = 95%) after 90 min at room temperature (Figure S23b, Supporting Information). However, despite having a larger η, the hydrogels were less elastic ($\epsilon_{max,original\ hydrogel}$ = 185%) than a self-healed gelatin–[MTEOA][$MeOSO_3$] ionogel. Thus the extent of self-healing for the gelatin–[MTEOA][$MeOSO_3$] is more than sufficient for on-skin electronic applications as the largest endured strain before breakage is significantly larger than that of a human's skin.[59]

The self-healing capability of the gelatin–[MTEOA][$MeOSO_3$] film was further demonstrated with a screen-printed PEDOT:PSS-based OECT. A cut was made across the solid electrolyte that effectively disconnects the channel and side-gate (Figure 4c). The transfer characteristics (Figure 4d) after cutting the OECT shows no gating effect. However, the OECT measured immediately after placing back together showed remarkable rapid self-healing with identical transfer characteristics as the uncut device. The rapid self-healing is mediated by the dynamic noncovalent hydrogen bonds formation.

The unique combination of the well-matched Young's modulus and good ionic conductivity enables gelatin–[MTEOA][$MeOSO_3$] to function as an electrode for on-skin electronic applications. Its tissue-like softness and high stretchability is ideal for interfacing wearable or implantable devices on nonzero Gaussian textured surfaces, such as the human skin or tissue as it can significantly enhance the conformability thus resulting in higher fidelity of signal transduction for biosensing and modulation. A thin and flexible gelatin–[MTEOA][$MeOSO_3$] film is attached on the wrist of a human as shown in Figure 4e. Good adhesion between gelatin and the skin or tissue can be attributed to the formation of interfacial covalent and noncovalent bonds such as imine, amide, or hydrogen bonds.[60] A reusable and flexible dry textile electrode (Ag-GMM) was fabricated by laminating a 60 µm gelatin–[MTEOA][$MeOSO_3$] layer onto conductive Ag-plated textile. The overall skin–electrode impedance obtained with the Ag-GMM textile electrodes is lower than commercial electrodes due to the reduced contact resistance from more conformal contact (Figure 4f). Weak epidermal biopotentials, such as electrocardiography (ECG) which are in the order of few millivolts, are particularly susceptible to noise

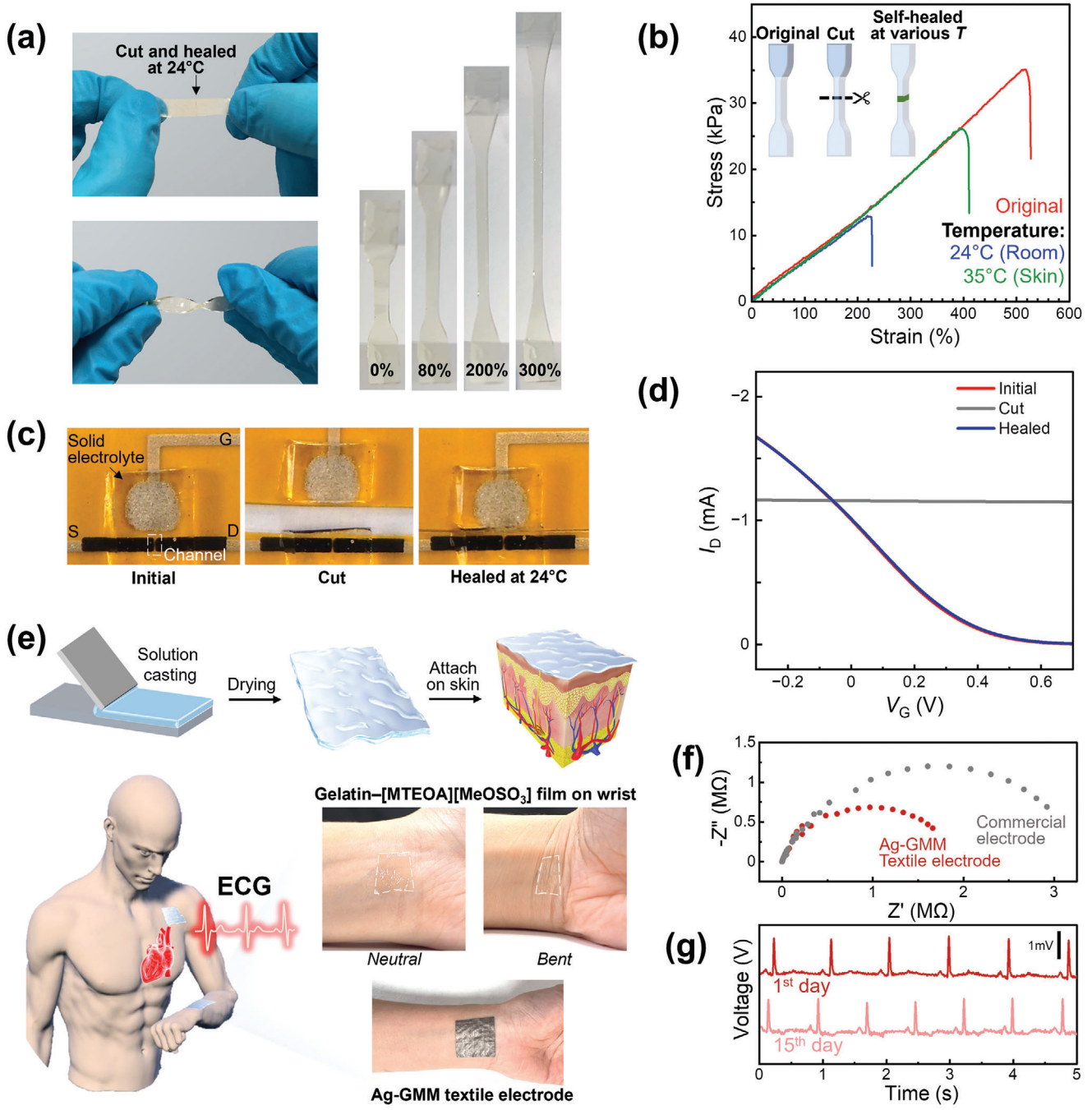

Figure 4. Flexible, stretchable, self-healable, and biocompatible gelatin–[MTEOA][$MeOSO_3$] solid electrolyte. a) A solid electrolyte cut into half and partially self-healed after placing back into contact at room temperature (left, top), and in a twisted position (left, bottom). Arrow indicates position of cut. A dumbbell-shaped solid electrolyte stretched to various extents (strain %) during tensile measurement. b) Stress–strain curve of the electrolytes before (original) and after being cut and self-healed at various temperatures. c) Screen-printed OECT on a polyimide substrate (left). A cut is made across the device, between the channel and the gate electrode (middle). The two halves are placed back together and the electrolyte is left to self-heal at room temperature (right). d) Transfer characteristics of the PEDOT:PSS-based screen-printed OECT ($W/L/d$ = 380 µm/75 µm/400 nm) before and after being cut. e) Schematic of the fabrication process of a gelatin–[MTEOA][$MeOSO_3$] solid electrolyte film—an aqueous gelatin— [MTEOA][$MeOSO_3$] solution is casted on a mold or substrate and annealed till dry. The resultant standalone film shows conformal contact on the skin (the dashed box guides the location of the film) and can be used as an interlayer between a conductive textile electrode and the skin for detection of physiological signals, such as electrocardiography (ECG). f) Nyquist plot of commercial electrodes (gray) and Ag textile coated gelatin–[MTEOA][MeOSO3] (Ag-GMM) electrodes (red) acquired on the skin surface of a human forearm. The impedance was measured between 0.1 Hz and 1 м Hz. g) ECG measurements demonstrating the ambient storage stability of the flexible Ag-GMM textile electrodes.

exacerbated by poor electrode-skin interface. Many commercial gel electrodes have limited shelf life and are not reusable as they dehydrate in ambient.[61] Dehydration increases the electrode impedance leading to reduced signal quality. In contrast, the Ag-GMM remained stable as evident from the repeatable ECG signals using electrodes that were stored in ambient and reused after 2 weeks (Figure 4g). The Ag-GMM does not suffer from dehydration issues as its high conductivity is provided by the nonvolatile IL in the matrix and does not rely on ion solvation due to hydration. The Ag-GMM electrodes can also be coupled to an OECT to provide amplification of the ECG signals (Figure S24, Supporting Information).

3. Conclusion

In summary, we proposed a new biocompatible, stretchable and flexible, self-healable solid electrolyte system, based on a blend of gelatin and [MTEOA][$MeOSO_3$] ionic liquid, that is compatible with a wide range of ionophilic and hydrophilic OMIECs for high-performance OECTs. We demonstrated high transconductance, fast transient response, and excellent electrochemical doping–dedoping cycling stability with gelatin–[MTEOA][$MeOSO_3$] which outperforms other state-of-the-art solid electrolytes. Furthermore, the nonvolatile gelatin–[MTEOA][$MeOSO_3$] system exhibited high and stable ionic conductivity that is relatively insensitive to the environment (across a range of humidities and high temperatures up to 120 °C). With a single solid electrolyte system capable of efficiently injecting ions into both *p*- and *n*-type OMIEC materials, we further demonstrated an ultralow-power, and to the best our knowledge, highest reported gain for an all-solid-state OECT-based complementary inverter. Combined with its self-healing, biocompatible, and stretchable properties, the proposed solid electrolyte system has the potential for application in high performance wearable organic electronics.

4. Experimental Section

Materials: Gelatin (48723), tris(2-hydroxyethyl)methylammonium methylsulfate [MTEOA][$MeOSO_3$], 1-ethyl-3-methylimidazolium tetrafluoroborate ([EMIM][BF_4]), 1-ethyl-3-methylimidazolium bis(trifluoromethylsulfonyl)imide ([EMIM][TFSI]), sodium chloride (NaCl), poly(vinylidene fluoride-*co*-hexafluoropropylene) (PVDF-*co*-HFP), (3-glycidyloxypropyl) trimethoxysilane (GOPS), ethylene glycol (EG), poly(benzimidazobenzophenanthroline) (BBL), poly(sodium 4-styrenesulfonate) (PSSNa) (molecular weight M_w = ≈1 M), poly(vinyl alcohol) (PVA) (M_w = ≈146–186k), poly(diallyldimethylammonium chloride) (PDADMAC) (M_w = ≈400–500 k), polyvinylpyrrolidone (PVP) (M_w = ≈1.3 M), poly(ethylene oxide) (PEO) (M_w = ≈100 k), methanesulfonic acid (MSA), dimethyl sulfoxide (DMSO), and chloroform were purchased from Sigma-Aldrich. Poly(3,4-ethylenedioxythiophene)-poly(styrenesulfonate) (PEDOT:PSS) (Clevios PH1000 and Clevios S V3) were purchased from Heraeus. Regioregular poly (3-(5-carboxypentyl)thiophene-2,5-diyl) (P3CPT) was purchased from Rieke Metals. Poly[(5-fluoro-2,1,3-benzothiadiazole-4,7-diyl) (4,4-dihexadecyl-4H-cyclopenta[2,1-*b*:3,4-*b*'] dithiophene-2,6-diyl) (6-fluoro-2,1,3-benzothiadiazole-4,7-diyl) (4,4-dihexadecyl-4H cyclopenta[2,1-*b*:3,4-*b*']dithiophene-2,6-diyl)] (PCDTFBT) was purchased from 1-materials. The ethylene glycol functionalized conjugated polymers poly(2-(3,3'-monoethyleneglycol monomethyl ether)-[2,2'-bithiophen]-5yl)-alt-(2-(3,3'-pentaethyleneglycol monomethyl ether)-[2,2'-bithiophen]-5yl) (p(g1T2-g5T2)),[42] poly(2-(4,4'-bis(2-methoxyethoxy)-5'-methyl-[2,2'bithiophen]-5-yl)-5-methylthieno[3,2-b]thiophene) (pgBTTT),[62] and poly(2,7-di(2,5,8,11-tetraoxaheptadecan-17-yl)-4-(thiophen-2-yl)benzo[lmn][3,8]phenanthroline-1,3,6,8(2H,7H)-tetraone) p(C_6NDI-T)[43] were synthesized by Prof. McCulloch's group based on previous reports. The silver/silver chloride (Ag/AgCl) ink (124-36) was purchased from Creative Materials. Silver (5028) and carbon (7102) screen-printing pastes were purchased from DuPont. Ultrapure type-I water (Sartorius Arium Mini Plus) were used for all experiments.

OECTs and Inverter Fabrication: *Parylene-patterned OECTs*. OECT source/drain/gate electrodes substrates were fabricated using a photolithography process on a SiO_2/Si substrate. AZ5214 photoresist was spin-coated on the precleaned substrate and soft-baked at 110 °C for 180 s before exposure to UV light (405 nm, 1.2 s) using a mask aligner (SUSS MicroTec MJB4) under a shadow mask. The substrates were subsequently baked at 110 °C for 180 s before flood exposure for 15 s and developed with AZ developer. 7 nm thick chromium followed by 50 nm thick gold were thermally evaporated onto the substrates. The substrates were subsequently immersed and sonicated in acetone. A 2 µm thick insulating parylene-C layer was first deposited with an adhesion promoter, A174 [3-(trimethoxysilyl)-propyl methacrylate], using Femtoscience Lavida 110. The substrate was subsequently spin-coated with a dilute soap solution (10% Micro-90 in water). Next, the substrate was coated with another 2.5 µm thick insulating parylene-C layer. A 12 µm thick AZ P4620 photoresist was subsequently spin-coated onto the substrate, soft-baked at 110 °C for 180 s, exposed to UV light, and developed with AZ developer. The patterned channel area and contact pads were etched via reactive ion etching (Oxford Plasmalab80) at 50 sccm O_2, 10 sccm CHF_3, 160 W operating conditions. Prior to OECT channel polymer film deposition, the substrates were rinsed with acetone, isopropanol, and dried with a nitrogen (N_2) gun, followed by air plasma for 10 min. *OECT channel*. The polymer films were prepared as follows: 36 nm thick BBL was deposited by spin-coating from a methanesulfonic acid solution in an N_2 glovebox, followed by immersing the films in acetonitrile for 15 min before annealing the films at 200 °C for 1 h. 35 nm thick P3CPT was deposited by spin-coating from a DMSO solution followed by annealing at 160 °C for 10 min in N_2. 53 nm thick PEDOT:PSS was deposited by spin-coating from a pre-filtered (0.45 µm polyethersulfone filter) solution comprising of PH1000 with 5 vol% EG and 0.5 vol.% GOPS followed by annealing at 140 °C for 10 min in air. 15 nm thick p(g1T2-g5T2), 34 nm thick p(C_6NDI-T), 47 nm thick pgBTTT, and 15 nm thick PCDTFBT were deposited by spin-coating from chloroform solution in an N_2 glovebox. *Planar side-gate*. Ag/AgCl ink was drop-casted in air onto the substates, followed by annealing at 100 °C for 5 min. *Electrolyte*. The solid electrolyte films were prepared as follows: Gelatin was mixed with water at a mass ratio of 1:2 gelatin:water and annealed at 80 °C, with occasional mixing using a planetary centrifugal mixer, till a complete dissolution. Different mass ratios of [MTEOA][$MeOSO_3$] ionic liquid (IL) (X wt%, where $X = \frac{\text{Mass of [MTEOA][MeOSO3]}}{\text{Mass of [MTEOA][MeOSO3]+Mass of dried gelatin}} \times 100\%$) were added to the gelatin aqueous solution and annealed at 80 °C with occasional mixing using a planetary centrifugal mixer till uniformly mixed. The gelatin or gelatin–[MTEOA][$MeOSO_3$] solutions were drop-casted onto the substrates in air from a warmed liquified solution at 80 °C. The films were annealed at 95 °C for 15 min followed by 130 °C for 15 min. PVDF-*co*-HFP was mixed with acetone at a mass ratio of 1:7 PVDF-*co*-HFP:acetone and annealed at 60 °C, with occasional mixing using a planetary centrifugal mixer, till a complete dissolution. [EMIM][TFSI] or [EMIM][BF_4] ILs, at a mass ratio 1:7:4 PVDF-*co*-HFP:acetone:IL, were added to the PVDF-*co*-HFP solutions and annealed at 60 °C with occasional mixing using a planetary centrifugal mixer till uniformly mixed. The cooled solutions were subsequently spin-coated in air onto the substrates. *Screen-printed OECTs*. PEDOT:PSS (Clevios S V3), which serves as the electrochemically active OECT channel, is screen printed on a flexible polyimide (PI) substrate and annealed at 140 °C for 5 min. Silver source, drain, and gate lead lines were subsequently screen-printed and annealed at 100 °C for 5 min. Next, carbon which overlaps the PEDOT:PSS channel and the silver lead lines, served as the source and drain electrodes, was screen-printed and

annealed at 100 °C for 5 min. Ag/AgCl, served as the gate electrode, was drop-casted onto the substates and annealed at 100 °C for 5 min. Finally, the gelatin–[MTEOA][$MeOSO_3$] (80 wt%) solution was drop-casted from a warmed liquified solution at 80 °C. The substrates were annealed at 95 °C for 15 min followed by 130 °C for 15 min. All devices were stored in dark ambient air (24 °C, 67% relative humidity) for minimally 16 h (overnight) before device measurement, unless otherwise specified.

Film thickness and OECT Channel Dimension Characterization: Polymer films were deposited using the same protocol alongside device fabrication on a separate SiO_2/Si substrate without the metal contacts. The thicknesses of the films were measured by a profilometer (KLA Alpha-step D500). The thicknesses of the gelatin or gelatin–[MTEOA][$MeOSO_3$] films were measured using profilometer or white light reflectance spectroscopy (Thetametrisis FR-pRo). The channel length (L) and width (W) for each device was individually measured using an optical microscope (Olympus Microscope BX53M).

OECT and Inverter Characterizations: The current–voltage (I–V) characteristics of the OECT devices including transfer curves, output curves, and transient measurements were carried out in dark ambient air using Keysight precision source/measure unit (B2912A). Threshold voltage (V_T) was determined by extrapolating the linear portion of the slope with the maximum magnitude from the forward scan of the plot of square root of the drain current ($\sqrt{I_D}$) vs gate voltage (V_G) in the saturation region. The intersection of the linear fit with the x-axis gives the V_T. Inverter characteristics including output, gain, power consumption, and transient measurements was sourced and measured by both Keysight B1500A and Keysight B2912A source meters. The transient characteristics typically shows a two-stage turn-on I_D.[63] that includes an initial delay attributed to a doping front propagation (t_p) followed by an exponential-like increase over time which often cannot be fitted using a single exponential function. The turn-off I_D, on the other hand, often follows a single exponential decay. Therefore, for quantitative comparison of the transient response, the off-to-on time (t_{on}) and on-to-off time (t_{off}) were obtained by the time taken for the change in I_D to increase or decrease by (1−1/e) = 0.632, respectively. A detailed example of the t_{on} and t_{off} extraction is described in Figure S21 (Supporting Information).

Polymer–[MTEOA][$MeOSO_3$] Ionogels: [MTEOA][$MeOSO_3$] was added to aqueous solutions of PSSNa, PVA, PDADMAC, PVP, and PEO at a mass ratio of 1:4 polymer:IL. The solutions were mixed using a planetary centrifugal mixer. Ionogels were obtained by drop-casting the solutions onto a substrate and annealing at 95 °C for 1 h to evaporate the water solvent.

Cyclic Voltammetry: The cyclic voltammetry measurements were performed using an electrochemical analyzer (Metrohm Autolab PGSTAT302N) with a three-terminal setup. Platinum was used as the working and counter electrode and Ag/AgCl pellet was used as a quasireference electrode. The [MTEOA][$MeOSO_3$] IL and 0.1 M aqueous NaCl solution were used as electrolytes. The potential was swept from −0.5 to 1.3 V with a scan rate of 20 mV s^{-1} under an ambient air environment around 24 °C.

OMIEC Volumetric Capacitance: Polymer films, served as the working electrode, were spin-coated on Au-patterned substrates following the same protocol described above. Ag/AgCl, served as the counter and reference electrode, was drop-casted onto the substates and annealed at 100 °C for 5 min. Finally, the gelatin–[MTEOA][$MeOSO_3$] (80 wt%) solid electrolyte film which overlaps the working electrode and counter/reference electrode was prepared following the same protocol described above. The volumetric capacitance (C^*) of the samples were determined by electrical impedance spectroscopic (EIS) measurements using an electrochemical analyzer (Metrohm Autolab PGSTAT302N) with a two-terminal setup (counter and reference electrode connected together to one electrode while working electrode connected to the other electrode) in a frequency range of 1–1M Hz with an alternating current (A.C.) modulation of 10 mV and a range of direct current (D.C.) offset voltages that corresponds to the same V_G range used in their corresponding transfer curves. The C^* values at each D.C. offset voltages were extracted from low frequency region of the spectrum (1 Hz), where the A.C. modulation is sufficiently slow to allow ions to populate. Finally, the reported C^* values were interpolated using a D.C. offset voltage that corresponds to the V_G at maximum transconductance (g_m) determined from the forward scans of the transfer plots.

ECG Measurement and Signal Processing: The Ag textile coated with gelatin–[MTEOA][$MeOSO_3$] (Ag-GMM) electrodes were prepared by laminating a 60 µm thick gelatin–[MTEOA][$MeOSO_3$] (80 wt%) films with dimensions of 1.6 × 1.6 cm^2 on a Ag-plated nylon textile (Ripstop silver fabric, LessEMF). Electrodes were placed on the left wrist and below the left breast along the anterior axillary line. Commercial gel electrodes (2239, 3M Red Dot monitoring electrodes, diameter of gel area was ≈1.8 cm) were also used for comparison. The signals were collected using Keysight precision source/measure unit (B2912A). To extract the relevant information in the ECG signal, the original ECG signal was digitally filtered using a low pass filter to remove the noise interference caused by the 50 Hz power line and electromagnetic radiation in the surrounding environment. The Ag-GMM electrodes placed in direct contact with the skin on the right wrist and below the left breast along the anterior axillary line were also connected to the source and gate contacts, respectively, of a PEDOT:PSS-based OECT. The ECG measurements were taken in compliance with the Institutional Review Board (approval number: IRB-2022-102) and informed written consent was obtained prior to subject participation.

Contact Impedance Measurement: Ag-GMM textile electrodes were prepared as described earlier. Two electrodes, used as the working and counter electrodes, were placed on the underside of the left forearm with a center-to-center distance of 10 cm. A commercial gel electrode, used as the reference electrode, was placed at the center of the two electrodes. The electrode-skin contact impedance was measured using an electrochemical analyzer (Metrohm Autolab PGSTAT302N) over a frequency range from 0.1 to 10k Hz. For comparison, the working and counter electrodes were replaced with commercial gel electrodes.

Electrolyte Ionic Conductivity: The ionic conductivity of the samples were determined by EIS measurements using an electrochemical analyzer with a two-terminal setup (counter and reference electrode connected together to one electrode, while working electrode connected to the other electrode) in a frequency range of 0.1–1M Hz with an A.C. modulation of 10 mV. Aqueous solutions of gelatin with different ratios of IL were spin-coated on 7 nm/50 nm thick Cr/Au-coated SiO_2 substrates. The films were annealed in ambient air at 95 °C for 15 min followed by 130 °C for 15 min. 50 nm thick Au was thermally evaporated to form the top ion-blocking electrode. The samples were equilibrated in ambient air for at least 24 h before measurement. The electrode/solid electrolyte/electrode assembly was mounted in a Linkam chamber with temperature controllable stage and incrementally annealed in ambient air from 25 to 120 °C. The samples were equilibrated for 3 min at each temperature set point before starting the measurements. At the end of the set of ambient measurements, the Linkam chamber was sealed and equilibrated in a N_2 environment for 1 h to cool before repeating the set of measurements in N_2 following the same procedure in ambient air. For measurements at different humidities, the sample was mounted in a Linkam chamber and its conductivity was first measured in air at room temperature (24 °C, relative humidity (R.H.) = 64%). The Linkam chamber was subsequently closed and purged with a continuous flow of N_2, while the sample was annealed at 100 °C for 1 h before cooling back to room temperature while in N_2. The conductivity was measured again at room temperature in N_2 (R.H. = 0%). Next, the N_2 gas was passed through a bubbler filled with saturated salt solutions—potassium hydroxide (relative humidity (R.H.) = 8%), magnesium chloride (R.H. = 33%), sodium bromide (R.H. = 57%), and potassium chloride (R.H. = 86%).[64,65] The humid N_2 gas was continuously passed through the sealed Linkam chamber for 30 min prior to the start of each measurement to allow for equilibration. The ionic conductivity σ was determined from the equation $\sigma = \frac{R_b A}{L}$, where the bulk resistance R_b is the frequency-independent real impedance corresponding to the minimum phase angle,[66] A is the area of the ion-blocking Au electrodes and L is the thickness of the solid electrolyte.

Fourier Transform Infrared (FTIR) Spectroscopy: The FTIR spectra of the samples were recorded on a PerkinElmer Frontier FTIR spectrometer, equipped with an attenuated total reflection (ATR) accessory, at room tem-

perature in the region of 4000–600 cm^{-1} with a resolution of 4 cm^{-1} and 8 scans.

Rheology: Rheology measurements were carried out with a MCR 702e rheometer (Anton Paar) using a 25 mm diameter plate–plate geometry. The mechanical spectra were recorded with a temperature-dependent oscillatory mode using a constant shear strain (γ) of 1% and an angular frequency (ω) of 10 rad s^{-1}. The gelatin–[MTEOA][$MeOSO_3$] (80 wt%) ionogel film was prepared following the same protocol described above. The gelatin–[MTEOA][$MeOSO_3$] (80 wt%) hydrogel and gelatin hydrogel films were prepared by casting a solution with mass ratios of 1:2:4 gelatin:water:[MTEOA][$MeOSO_3$] and 1:4 gelatin:water, respectively, into an airtight container and storing at 4 °C for 1 h to solidify before leaving in room temperature (24 °C) overnight prior to the measurement. The films were placed on an isothermal plate of the rheometer that was maintained at 20 °C at the start of the measurement and temperature was ramped up to 65 °C at a rate of 2.5 °C min^{-1}. The melting temperature (T_m) was determined by the crossover point where the storage modulus (G') is equals to the loss modulus (G'') as the films changes from a solid-to-liquid state.

Differential Scanning Calorimetry (DSC): Calorimetric measurements were performed using a TA Instruments Q10 DSC. Aqueous solutions of gelatin with different ratios of IL were casted on hermetic aluminum pans and annealed at 90 °C for 15 min followed by 130 °C for 15 min. The dried mass of the samples (about 5−15 mg) were determined immediately after heating. The samples were equilibrated in ambient for at least 24 h before crimping. Measurements were carried out by cooling the samples to −20 °C before heating at a rate of 2 °C min^{-1} with N_2 as the purge gas. An empty sealed hermetic aluminum pan was used as reference. The glass transition temperature (T_g) was estimated from the onset value of the corresponding endothermic event. The value of enthalpy was calculated with respect to the dried mass of the gelatin-IL composites.

Tensile Test: A tensile tester (ESM-303, Mark-10 Corporation) with a force gauge (M5I, Mark-10) was equipped with a 2.5 N force sensor (MR03-05, Mark 10). Gelatin−[MTEOA][$MeOSO_3$] ionogel samples was prepared following the same protocol described above and used for determining the extent of self-healing at different temperatures and fatigue resistance test. The samples were cut into a standard type 3 dumbbell with a test gauge length (L_0) of 10 mm, width (W_0) of 4 mm, and thickness (d_0) of ≈1 mm. Samples for testing self-healing were cut in half and placed back into contact at room temperature (24 °C) or at skin surface temperature (35 °C) for 1 h before being tested 72 h later. The stress–strain behavior was measured by stretching the sample at a fixed speed of 25 mm min^{-1}. Fatigue resistance test was performed at a speed of 100 mm min^{-1}. To study the effect of bulk water on extent of self-healing and self-healing time required, gelatin−[MTEOA][$MeOSO_3$] hydrogel samples were prepared by casting a solution with mass ratios of 1:2:4 gelatin:water:[MTEOA][$MeOSO_3$] into an airtight container and storing at 4 °C for 1 h before leaving in room temperature (24 °C) for 30 min prior to being cut and tested. Gelatin−[MTEOA][$MeOSO_3$] ionogel samples was prepared following the same protocol described above. The samples were cut into a standard type 4 dumbbell with a L_0 of 12 mm, width W_0 of 2 mm, and d_0 of ≈2.5 mm. Samples for testing self-healing were cut in half and placing back into contact at room temperature (24 °C) for 20 and 90 min before being immediately tested. The stress–strain behavior was measured by stretching the sample at a fixed speed of 25 mm min^{-1}.

Computational Methodologies: The geometries of the cations and anions were first optimized using DFT/B3LYP/6-31++G(d,p) calculations until no imaginary frequencies were found. The size of the ions were determined by measuring the largest distances of the atoms within the molecule, including its Van Der Waals radius.

Supporting Information

Supporting Information is available from the Wiley Online Library or from the author.

Acknowledgements

This work was supported by the Ministry of Education (MOE) under AcRF Tier 2 grant (MOE2019-T2-2-106) and AcRF Tier 1 grant (RG118/21). C.G.T. acknowledged funding support from her NTU Presidential Postdoctoral Fellowship (PPF).

Conflict of Interest

The authors declare no conflict of interest.

Data Availability Statement

The data that support the findings of this study are available from the corresponding author upon reasonable request.

Keywords

bioelectronics, flexible electronics, inverter, ionogels, organic electrochemical transistors

Received: April 18, 2024
Revised: June 20, 2024
Published online:

[1] P. Andersson Ersman, D. Westerberg, D. Tu, M. Nilsson, J. Åhlin, A. Eveborn, A. Lagerlöf, D. Nilsson, M. Sandberg, P. Norberg, M. Berggren, R. Forchheimer, G. Gustafsson, *Flex. Print. Electron.* **2017**, *2*, 045008.
[2] B. Schmatz, A. W. Lang, J. R. Reynolds, *Adv. Funct. Mater.* **2019**, *29*, 1905266.
[3] W. Huang, J. Chen, Y. Yao, D. Zheng, X. Ji, L. W. Feng, D. Moore, N. R. Glavin, M. Xie, Y. Chen, R. M. Pankow, A. Surendran, Z. Wang, Y. Xia, L. Bai, J. Rivnay, J. Ping, X. Guo, Y. Cheng, T. J. Marks, A. Facchetti, *Nature* **2023**, *613*, 496.
[4] H. Lee, S. Lee, W. Lee, T. Yokota, K. Fukuda, T. Someya, *Adv. Funct. Mater.* **2019**, *29*, 1906982.
[5] S. Chen, A. Surendran, X. Wu, W. L. Leong, *Adv. Funct. Mater.* **2020**, *30*, 2006186.
[6] R. Granelli, I. Alessandri, P. Gkoupidenis, I. Vassalini, Z. M. Kovacs-Vajna, P. W. M. Blom, F. Torricelli, *Small* **2022**, *18*, e2108077.
[7] P. C. Harikesh, C. Y. Yang, D. Tu, J. Y. Gerasimov, A. M. Dar, A. Armada-Moreira, M. Massetti, R. Kroon, D. Bliman, R. Olsson, E. Stavrinidou, M. Berggren, S. Fabiano, *Nat. Commun.* **2022**, *13*, 901.
[8] X. Su, X. Wu, S. Chen, A. M. Nedumaran, M. Stephen, K. Hou, B. Czarny, W. L. Leong, *Adv. Mater.* **2022**, *34*, 2200682.
[9] S. T. M. Tan, S. Keene, A. Giovannitti, A. Melianas, M. Moser, I. McCulloch, A. Salleo, *J. Mater. Chem. C* **2021**, *9*, 12148.
[10] K. Guo, S. Wustoni, A. Koklu, E. Diaz-Galicia, M. Moser, A. Hama, A. A. Alqahtani, A. N. Ahmad, F. S. Alhamlan, M. Shuaib, A. Pain, I. McCulloch, S. T. Arold, R. Grunberg, S. Inal, *Nat. Biomed. Eng.* **2021**, *5*, 666.
[11] P. Li, T. Lei, *J. Polym. Sci.* **2021**, *60*, 377.
[12] Y. He, N. A. Kukhta, A. Marks, C. K. Luscombe, *J. Mater. Chem. C* **2022**, *10*, 2314.
[13] N. A. Kukhta, A. Marks, C. K. Luscombe, *Chem. Rev.* **2022**, *122*, 4325.
[14] J. Tropp, J. Rivnay, *J. Mater. Chem. C* **2021**, *9*, 13543.
[15] J. Tropp, D. Meli, J. Rivnay, *Matter* **2023**, *10*, 3132.
[16] C. Cendra, A. Giovannitti, A. Savva, V. Venkatraman, I. McCulloch, A. Salleo, S. Inal, J. Rivnay, *Adv. Funct. Mater.* **2019**, *29*, 1807034.

[17] J. Wagner, Y. Song, T. Lee, H. E. Katz, *Electrochem. Sci. Adv.* **2021**, *2*, e2100165.
[18] M. Moser, Y. Wang, T. C. Hidalgo, H. Liao, Y. Yu, J. Chen, J. Duan, F. Moruzzi, S. Griggs, A. Marks, N. Gasparini, A. Wadsworth, S. Inal, I. McCulloch, W. Yue, *Mater. Horiz.* **2022**, *9*, 973.
[19] Y. Wang, E. Zeglio, L. Wang, S. Cong, G. Zhu, H. Liao, J. Duan, Y. Zhou, Z. Li, D. Mawad, A. Herland, W. Yue, I. McCulloch, *Adv. Funct. Mater.* **2022**, *32*, 2111439.
[20] Y. Wang, G. Zhu, E. Zeglio, T. C. H. Castillo, S. Haseena, M. K. Ravva, S. Cong, J. Chen, L. Lan, Z. Li, A. Herland, I. McCulloch, S. Inal, W. Yue, *Chem. Mater.* **2023**, *35*, 405.
[21] A. S. Sharova, F. Modena, A. Luzio, F. Melloni, P. Cataldi, F. Viola, L. Lamanna, N. F. Zorn, M. Sassi, C. Ronchi, J. Zaumseil, L. Beverina, M. R. Antognazza, M. Caironi, *Nanoscale* **2023**, *15*, 10808.
[22] Y. J. Jo, K. Y. Kwon, Z. U. Khan, X. Crispin, T. I. Kim, *ACS Appl. Mater. Interfaces* **2018**, *10*, 39083.
[23] T. Nguyen-Dang, K. Harrison, A. Lill, A. Dixon, E. Lewis, J. Vollbrecht, T. Hachisu, S. Biswas, Y. Visell, T. Q. Nguyen, *Adv. Electron. Mater.* **2021**, *7*, 2100519.
[24] X. Wu, S. Chen, M. Moser, A. Moudgil, S. Griggs, A. Marks, T. Li, I. McCulloch, W. L. Leong, *Adv. Funct. Mater.* **2022**, *33*, 2209354.
[25] H. H. Chouhdry, D. H. Lee, A. Bag, N.-E. Lee, *Nat. Commun.* **2023**, *14*, 821.
[26] S. Y. Jeong, J. W. Moon, S. Lee, Z. Wu, S. H. Park, J. H. Cho, H. Y. Woo, *Adv. Electron. Mater.* **2023**, *9*, 2300053.
[27] K. Hou, S. Chen, A. Moudgil, X. Wu, T. L. D. Tam, W. S. Lew, W. L. Leong, *ACS Appl. Electron. Mater.* **2023**, *5*, 2215.
[28] D. Khodagholy, V. F. Curto, K. J. Fraser, M. Gurfinkel, R. Byrne, D. Diamond, G. G. Malliaras, F. Benito-Lopez, R. M. Owens, *J. Mater. Chem.* **2012**, *22*, 4440.
[29] A. Weissbach, L. M. Bongartz, M. Cucchi, H. Tseng, K. Leo, H. Kleemann, *J. Mater. Chem. C* **2022**, *10*, 2656.
[30] Y. Zhong, N. Lopez-Larrea, M. Alvarez-Tirado, N. Casado, A. Koklu, A. Marks, M. Moser, I. McCulloch, D. Mecerreyes, S. Inal, *Chem. Mater.* **2024**, *36*, 1841.
[31] C. Y. Yang, D. Tu, T. P. Ruoko, J. Y. Gerasimov, H. Y. Wu, P. C. Harikesh, M. Massetti, M. A. Stoeckel, R. Kroon, C. Müller, M. Berggren, S. Fabiano, *Adv. Electron. Mater.* **2021**, *8*, 2100907.
[32] M. Massetti, S. Zhang, P. C. Harikesh, B. Burtscher, C. Diacci, D. T. Simon, X. Liu, M. Fahlman, D. Tu, M. Berggren, S. Fabiano, *Npj Flex Electron.* **2023**, *7*, 11.
[33] C. H. Kim, M. Azimi, J. Fan, H. Nagarajan, M. Wang, F. Cicoira, *Nanoscale* **2023**, *15*, 3263.
[34] M. Zabihipour, D. Tu, R. Forchheimer, J. Strandberg, M. Berggren, I. Engquist, *Adv. Mater. Technol.* **2022**, *7*, 2101642.
[35] J. Guo, L. Q. Flagg, D. K. Tran, S. E. Chen, R. Li, N. B. Kolhe, R. Giridharagopal, S. A. Jenekhe, L. J. Richter, D. S. Ginger, *J. Am. Chem. Soc.* **2023**, *145*, 1866.
[36] S. Yu, C. J. Kousseff, C. B. Nielsen, *Synth. Met.* **2023**, *293*, 117295.
[37] M. G. Freire, C. M. S. S. Neves, I. M. Marrucho, J. A. P. Coutinho, A. M. Fernandes, *J. Phys. Chem. A* **2010**, *114*, 3744.
[38] X. Fan, S. Liu, Z. Jia, J. J. Koh, J. C. C. Yeo, C.-G. Wang, N. E. Surat'man, X. J. Loh, J. Le Bideau, C. He, Z. Li, T.-P. Loh, *Chem. Soc. Rev.* **2023**, *52*, 2497.
[39] T. Li, J. Y. Cheryl Koh, A. Moudgil, H. Cao, X. Wu, S. Chen, K. Hou, A. Surendran, M. Stephen, C. Tang, C. Wang, Q. J. Wang, C. Y. Tay, W. L. Leong, *ACS Nano* **2022**, *16*, 12049.
[40] J. E. Eastoe, *Biochem. J.* **1955**, *61*, 589.
[41] D. A. Bernards, G. G. Malliaras, *Adv. Funct. Mater.* **2007**, *17*, 3538.
[42] M. Moser, T. C. Hidalgo, J. Surgailis, J. Gladisch, S. Ghosh, R. Sheelamanthula, Q. Thiburce, A. Giovannitti, A. Salleo, N. Gasparini, A. Wadsworth, I. Zozoulenko, M. Berggren, E. Stavrinidou, S. Inal, I. McCulloch, *Adv. Mater.* **2020**, *32*, 2002748.
[43] A. Koklu, S. Wustoni, V. E. Musteata, D. Ohayon, M. Moser, I. McCulloch, S. P. Nunes, S. Inal, *ACS Nano* **2021**, *15*, 8130.
[44] M. Xie, H. Liu, M. Wu, C. Chen, J. Wen, L. Bai, J. Yu, W. Huang, *Org. Electron.* **2023**, *117*, 106777.
[45] A. Savva, R. Hallani, C. Cendra, J. Surgailis, T. C. Hidalgo, S. Wustoni, R. Sheelamanthula, X. Chen, M. Kirkus, A. Giovannitti, A. Salleo, I. McCulloch, S. Inal, *Adv. Funct. Mater.* **2020**, *30*, 1907657.
[46] W. Wang, Z. Li, M. Li, L. Fang, F. Chen, S. Han, L. Lan, J. Chen, Q. Chen, H. Wang, C. Liu, Y. Yang, W. Yue, Z. Xie, *Nano-Micro Lett.* **2022**, *14*, 184.
[47] M. Azimi, C.-h. Kim, J. Fan, F. Cicoira, *Faraday Discuss.* **2023**, *246*, 540.
[48] P. Romele, M. Ghittorelli, Z. M. Kovacs-Vajna, F. Torricelli, *Nat. Commun.* **2019**, *10*, 3044.
[49] K. J. Payne, A. Veis, *Biopolymers* **1988**, *27*, 1749.
[50] N. R. Dhumal, H. J. Kim, J. Kiefer, *J. Phys. Chem. A* **2011**, *115*, 3551.
[51] L. Portilla, K. Loganathan, H. Faber, A. Eid, J. G. D. Hester, M. M. Tentzeris, M. Fattori, E. Cantatore, C. Jiang, A. Nathan, G. Fiori, T. Ibn-Mohammed, T. D. Anthopoulos, V. Pecunia, *Nat. Electron.* **2023**, *6*, 10.
[52] P. C. Harikesh, C.-Y. Yang, H.-Y. Wu, S. Zhang, M. J. Donahue, A. S. Caravaca, J.-D. Huang, P. S. Olofsson, M. Berggren, D. Tu, S. Fabiano, *Nat. Mater.* **2023**, *22*, 242.
[53] Y. Yao, W. Huang, J. Chen, G. Wang, H. Chen, X. Zhuang, Y. Ying, J. Ping, T. J. Marks, A. Facchetti, *Proc. Natl. Acad. Sci. USA* **2021**, *118*, e2111790118.
[54] H. Y. Wu, C. Y. Yang, Q. Li, N. B. Kolhe, X. Strakosas, M. A. Stoeckel, Z. Wu, W. Jin, M. Savvakis, R. Kroon, D. Tu, H. Y. Woo, M. Berggren, S. A. Jenekhe, S. Fabiano, *Adv. Mater.* **2021**, *34*, 2106235.
[55] Z. Zhou, X. Wu, T. L. D. Tam, C. G. Tang, S. Chen, K. Hou, T. Li, Q. He, J. J. Sit, J. Xu, W. L. Leong, *Adv. Funct. Mater.* **2023**, *34*, 2305780.
[56] H. Y. Wu, J. D. Huang, S. Y. Jeong, T. Liu, Z. Wu, T. van der Pol, Q. Wang, M. A. Stoeckel, Q. Li, M. Fahlman, D. Tu, H. Y. Woo, C. Y. Yang, S. Fabiano, *Mater. Horiz.* **2023**, *10*, 4213.
[57] P. Andersson Ersman, R. Lassnig, J. Strandberg, D. Tu, V. Keshmiri, R. Forchheimer, S. Fabiano, G. Gustafsson, M. Berggren, *Nat. Commun.* **2019**, *10*, 5053.
[58] D. Hardman, T. George Thuruthel, F. Iida, *NPG Asia Mater* **2022**, *14*, 11.
[59] A. Ní Annaidh, K. Bruyère, M. Destrade, M. D. Gilchrist, M. Otténio, *J. Mech. Behav. Biomed. Mater.* **2012**, *5*, 139.
[60] S. Li, Y. Cong, J. Fu, *J. Mater. Chem. B* **2021**, *9*, 4423.
[61] A. Gruetzmann, S. Hansen, J. Müller, *Physiol. Meas.* **2007**, *28*, 1375.
[62] R. K. Hallani, B. D. Paulsen, A. J. Petty 2nd, R. Sheelamanthula, M. Moser, K. J. Thorley, W. Sohn, R. B. Rashid, A. Savva, S. Moro, J. P. Parker, O. Drury, M. Alsufyani, M. Neophytou, J. Kosco, S. Inal, G. Costantini, J. Rivnay, *J. Am. Chem. Soc.* **2021**, *143*, 11007.
[63] J. Guo, S. E. Chen, R. Giridharagopal, C. G. Bischak, J. W. Onorato, K. Yan, Z. Shen, C.-Z. Li, C. K. Luscombe, D. S. Ginger, *Nat. Mater.* **2024**, *23*, 656.
[64] L. B. Rockland, *Anal. Chem.* **1960**, *32*, 1375.
[65] L. Greenspan, *J. Res. Natl. Bur. Stand. A: Phys. Chem.* **1977**, *81A*, 89.
[66] X. Qian, N. Gu, Z. Cheng, X. Yang, E. Wang, S. Dong, *J. Solid State Electrochem.* **2001**, *6*, 8.